Diverging nematic susceptibility, physical meaning of T^* scale, and pseudogap in the spin fermion model for the pnictides

Shuhua Liang,[1,2] Anamitra Mukherjee,[2] Niravkumar D. Patel,[2] Christopher B. Bishop,[2] Elbio Dagotto,[1,2] and Adriana Moreo[1,2]
[1]*Materials Science and Technology Division, Oak Ridge National Laboratory, Oak Ridge, Tennessee 37831, USA*
[2]*Department of Physics and Astronomy, University of Tennessee, Knoxville, Tennessee 37996, USA*
(Received 23 May 2014; revised manuscript received 20 October 2014; published 12 November 2014)

Using Monte Carlo simulations with a tunable uniaxial strain, the nematic susceptibility of the spin fermion model for the pnictides is calculated. The results are in excellent agreement with the experiments by Chu *et al.* [Science **337**, 710 (2012)]. Via a Ginzburg-Landau analysis, our study suggests a nematicity in the spin fermion model primarily originating in magnetism, but with the lattice/orbital also playing a key role by boosting up critical temperatures and separating the structural T_S and Néel T_N transitions. At $T > T_S$, Curie-Weiss behavior is observed with a characteristic temperature T^* being the T_N of the purely electronic system. In this temperature regime, short-range magnetic order with wave vectors $(\pi,0)$-$(0,\pi)$ induce local nematic fluctuations and a density-of-states pseudogap, compatible with several experiments. The present analysis relies on the study of a particular model for the iron superconductors; thus further studies are needed to conclusively establish the driver of nematicity in real materials.

DOI: 10.1103/PhysRevB.90.184507 PACS number(s): 74.70.Xa, 71.10.Fd, 74.25.−q

I. INTRODUCTION

The complexity of high critical temperature iron-based superconductors [1,2], with coupled spin, charge, orbital, and lattice degrees of freedom, creates exotic regimes such as the widely discussed nematic state with broken rotational invariance [3,4]. This state may originate in the spin [5–9] or in the orbital [10–13] degrees of freedom, but subtleties in experiments (with strain required to detwin crystals) and in theory (employing complicated multiorbital models) have prevented the identification of the primary driver of the nematic regime.

Recent efforts to study nematicity have considered models with electrons coupled to the lattice [14]. The electronic sector is itself separated into itinerant and localized electrons defining a spin fermion (SF) model [15–18], compatible with the growing evidence that iron superconductors display a mixture of itinerant and localized features [2,19,20]. These studies unmasked a considerable electron-lattice feedback, leading to several results in agreement with experiments, such as anisotropic resistivities and a nematic and structural (tetragonal-orthorhombic) transition at T_S, slightly separated from the Néel temperature T_N ($<T_S$) [21].

More recently, a remarkable experimental development has been the report of a diverging nematic susceptibility $\chi^{\rm exp}$ vs temperature T, with a mysterious characteristic temperature scale T^*, for single crystals of $Ba(Fe_{1-x}Co_x)_2As_2$ [22] measured by varying an *in situ* uniaxial strain. Although contrasting $\chi^{\rm exp}$ against theory and explaining the physical meaning of T^* are crucial aspects to identify the mechanism that drives nematicity, to our knowledge $\chi^{\rm exp}$ and T^* have not been addressed theoretically before since temperatures above T_S are difficult to study with reliable methods.

In this publication, this nematic susceptibility is theoretically calculated via the spin fermion model coupled to the lattice in precisely the same setup as in Ref. [22]. Note that this susceptibility, which tests a local geometric property of an enlarged parameter space, is different from the simpler magnetic susceptibility calculated in Ref. [14] obtained from thermal statistics. The present computational effort required an order of magnitude more work than in Ref. [14] because the strain is an extra parameter to vary, rather than being dynamically adjusted in the Monte Carlo (MC) process as before. To implement this demanding task, modifications in the MC algorithm were introduced, as explained below. Compared to Hubbard multiorbital approaches, a unique characteristic of the spin fermion model is that simulations can be carried out in the nematic regime above the ordering temperatures. Remarkably, our susceptibility is very similar to the diverging experimental $\chi^{\rm exp}$ result. Moreover, we observed that the T^* scale in the Curie-Weiss behavior is the preexisting Néel critical temperature of the purely electronic sector, which is independent of the lattice. We also observed a density-of-states pseudogap and nematic fluctuations above T_S, caused by short-range $(\pi,0)$-$(0,\pi)$ antiferromagnetic order.

The paper is organized as follows: the model is introduced in Sec. II; the many-body techniques developed for this work as well as the main results are presented in Sec. III; the results for the spin-nematic and orbital-nematic susceptibilities are analyzed in Sec. IV, while the dependence on the structural transition temperature with the orbital-lattice coupling is discussed in Sec. V. The analysis of the spin structure factors and the pseudogap in the density of states is presented in Sec. VI. Section VII is devoted to the conclusions and the Appendix contains the full Hamiltonian, the numerically guided Ginzburg-Landau calculations, the comparison between total and partial derivatives at the critical temperature T_S, and numerical results for an unphysically large value of the lattice-orbital coupling.

II. MODELS

The model employed here combines the purely electronic spin fermion model [15–18] together with lattice orthorhombic distortions:

$$H_{\rm SF} = H_{\rm Hopp} + H_{\rm Hund} + H_{\rm Heis} + H_{\rm SL} + H_{\rm OL} + H_{\rm Stiff}. \quad (1)$$

 ©2014 American Physical Society

This (lengthy) full Hamiltonian is presented in the Appendix. $H_{\rm Hopp}$ is the Fe-Fe hopping of the d_{xz}, d_{yz}, and d_{xy} electrons (a three orbitals model is used with an electronic bandwidth $W \sim 3$ eV), with amplitudes that reproduce photoemission results. The average number of electrons per itinerant orbital is $n = 4/3$ [23]; i.e., the undoped regime will be our focus. This is reasonable since many experiments that address the nematic state are carried out for the parent compounds. Moreover, technically the study simplifies in the absence of doping and quenched disorder.

The Hund interaction is canonical: $H_{\rm Hund} = -J_{\rm H} \sum_{\mathbf{i},\alpha} \mathbf{S_i} \cdot \mathbf{s}_{\mathbf{i},\alpha}$, with $\mathbf{S_i}$ ($\mathbf{s}_{\mathbf{i},\alpha}$) the localized (itinerant with orbital index α) spin. $H_{\rm Heis}$ is the Heisenberg interaction among the localized spins involving nearest-neighbor (NN) and next-NN (NNN) interactions with couplings $J_{\rm NN}$ and $J_{\rm NNN}$, respectively, and ratio $J_{\rm NNN}/J_{\rm NN} = 2/3$ [17] to favor collinear order.

Within the spin-driven scenario for nematicity, the state between T_N and T_S is characterized by short-range spin correlations that have as an order parameter $\Psi_{\mathbf{i}} = \sum_{\pm}(\mathbf{S_i} \cdot \mathbf{S}_{\mathbf{i}\pm\mathbf{y}} - \mathbf{S_i} \cdot \mathbf{S}_{\mathbf{i}\pm\mathbf{x}})/2$ that satisfies $\langle\Psi\rangle > 0$ [9,24], where $\mathbf{S_i}$ is the spin of the iron atom at site $\mathbf{i}$ and $\mathbf{x}$,$\mathbf{y}$ are unit vectors along the axes. As described in the Appendix the $\mathcal{O}_{rth}$ distortion $\epsilon_{\mathbf{i}}$ associated with the elastic constant c_{66} will be considered here. The coupling of the spin-nematic order and the lattice is $H_{\rm SL} = -g \sum_{\mathbf{i}} \Psi_{\mathbf{i}}\epsilon_{\mathbf{i}}$ [8,9], where g is the lattice-spin coupling [25]. To also incorporate orbital fluctuations, the term $H_{\rm OL} = -\lambda \sum_{\mathbf{i}} \Phi_{\mathbf{i}}\epsilon_{\mathbf{i}}$ is added, where λ is the orbital-lattice coupling, $\Phi_{\mathbf{i}} = n_{\mathbf{i},xz} - n_{\mathbf{i},yz}$ is the orbital order parameter, and $n_{\mathbf{i},\alpha}$ the electronic density at site $\mathbf{i}$ and orbital α [13]. Finally, $H_{\rm Stiff}$ is the spin stiffness given by a Lennard-Jones potential that speeds up convergence as described in the Appendix.

III. MANY-BODY TECHNIQUES AND MAIN RESULTS

The Monte Carlo method used in this study is well known [17,18], and details will not be repeated. However, here an extra computational component had to be introduced because, compared with [14], for each temperature T now the strain was varied as an extra parameter. Since for each temperature typically 15 values of strain were used, this effort is ∼15 times more costly than in Ref. [14]. While the standard Monte Carlo is time consuming because of the fermionic-sector exact diagonalization (ED) at every step, in the related double-exchange models for manganites an improvement has been used before: the "traveling cluster approximation" (TCA) [26], where the MC updates are decided employing a cluster centered at site $\mathbf{i}$ but with a size substantially smaller than the full lattice size [27]. In addition, twisted boundary conditions (TBC) were also used [28]; here TCA and TBC are employed together. To simplify further the analysis, most couplings are fixed to values that were used successfully before [17]: $J_{\rm H} = 0.1$ eV, $J_{\rm NN} = 0.012$ eV, and $J_{\rm NNN} = 0.008$ eV. Dimensionless versions of the electron-lattice couplings are constructed via the definitions $\tilde{g} = 2g/\sqrt{kW}$ and $\tilde{\lambda} = 2\lambda/\sqrt{kW}$, as discussed in Ref. [14]. Here, $W = 3$ eV is the electronic bandwidth and k regulates the spin stiffness, as shown in the Appendix. These dimensionless constants are fixed to the values 0.16 and 0.12, respectively, that before [14] were found to be realistic. However, results for other values of these couplings are provided in the Appendix as well.

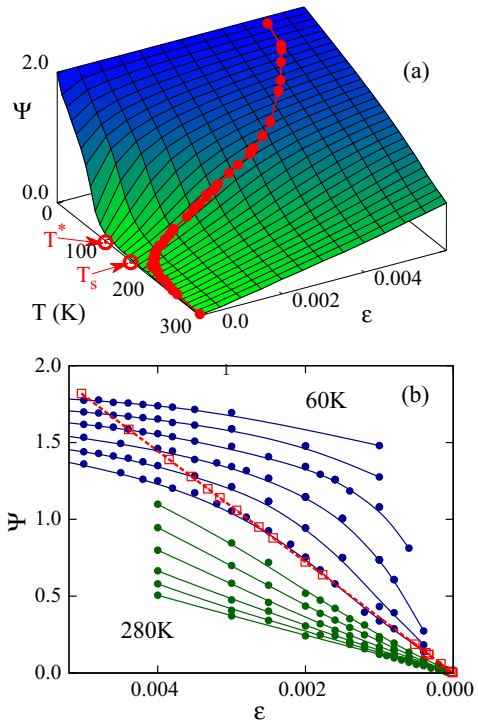

FIG. 1. (Color online) Monte Carlo spin-nematic order parameter, at $\tilde{g} = 0.16$ and $\tilde{\lambda} = 0.12$. (a) Ψ vs T and ϵ, measured at a fixed lattice distortion ϵ for each temperature (restricted MC). Shown are the T^* (see text) and T_S ($\sim T_N$) temperatures. Data are for an 8×8 cluster with TCA+TBC (PBC 8×8 clusters with ED give similar results). Red points are the equilibrium values using unrestricted MC with ED and PBC 8×8 clusters. (b) Ψ vs ϵ at fixed temperatures, illustrating their nearly linear relation in unrestricted MC (red), and also the linear slopes of the restricted MC curves (green/blue) close to T_S. Results are obtained with ED/PBC 8×8 clusters. Note that the number of green/blue points vastly outnumbers the number of red points, highlighting how much more demanding this effort has been than in Ref. [14].

The spin nematic susceptibility calculated here is defined as $\chi_s = \frac{\partial\Psi}{\partial\epsilon}|_{\epsilon_0}$, where ϵ_0 is the value of the lattice distortion obtained from the "unrestricted" numerical simulation where the lattice is equilibrated together with the spins, as in Ref. [14]. To calculate the susceptibility χ_s of our model, a procedure similar to the experimental setup was employed: the order parameter Ψ was measured at various temperatures and at fixed values of the lattice distortion $\epsilon = (a_x - a_y)/(a_x + a_y)$. In this publication, this procedure will be called "restricted" MC (note that this dimensionless ϵ should not be confused with the dimensionful $\epsilon_{\mathbf{i}}$ used in the Hamiltonian and defined in the Appendix). By this procedure, $\Psi(\tilde{g},\tilde{\lambda},T,\epsilon)$ are obtained at fixed couplings, defining surfaces as those shown in Fig. 1(a). Allowing the lattice to relax, the equilibrium curve that is shown with red points in Fig. 1(a) is obtained.

Figure 1(b) contains the (restricted) MC measured spin-nematic order parameter versus the (fixed) lattice distortion ϵ, at various temperatures. In a wide range of temperatures, a robust linear behavior is observed and χ_s can be easily extracted

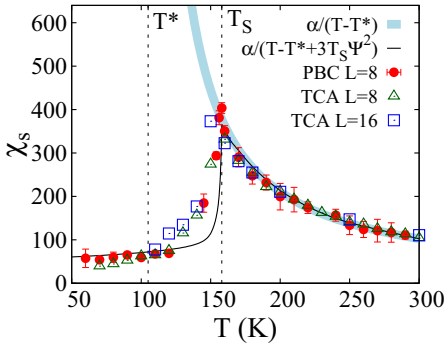

FIG. 2. (Color online) Nematic susceptibility χ_s of the spin fermion model vs temperature T (circles, triangles, and squares) obtained from Fig. 1(b), at the realistic couplings $\tilde{g} = 0.16$ and $\tilde{\lambda} = 0.12$ ($\alpha = \tilde{g}/a_0$). Two MC techniques were employed: "PBC $L = 8$" is the standard MC method with ED in the fermions at every step, using 8×8 clusters with PBC. "TCA $L = 8$" and "TCA $L = 16$" correspond to the TCA+TBC method on $L \times L$ clusters. Size effects are small. Also shown are two GL fits: the light blue (thick) line displays the Curie-Weiss equation $\chi_s \approx \frac{\tilde{g}}{a_0(T-T^*)}$, indicating a divergence at a lower temperature T^*, characteristic of the electronic sector alone. At $T \leqslant T_S$, the lattice follows the electronic sector. The black (thin) line is Eq. (A40) with the $3T_S\Psi^2$ correction (see text) [29].

numerically. Figure 1(b) is similar to the experimental results in Fig. 2A of Ref. [22]. The equilibrium result with both spins and lattice optimized (unrestricted MC) is also shown (red squares).

Our main result is presented in Fig. 2, where the numerically calculated χ_s vs T is displayed, at the realistic couplings used in previous investigations [14]. In remarkable agreement with experiments, χ_s grows when cooling down and it develops a sharp peak at T_S (compare with Fig. 2B of Ref. [22]). These results were obtained via two different procedures (standard ED and the TCA+TBC), and for two lattice sizes, indicating that systematic errors (such as size effects) are small.

IV. NEMATIC SUSCEPTIBILITY

A. Analysis of χ_s results

Supplementing the computational results, here Ginzburg-Landau (GL) calculations were also performed, similarly as in Ref. [22] for experiments. Note that the previous GL analysis considered only a generic nematic order parameter while our study separates the spin and orbital contributions. The rather complex numerical results presented in previous sections can be rationalized intuitively by this procedure. The results for χ_s (Fig. 2) are well fitted quantitatively for $T > T_S$, and qualitatively for $T < T_S$, by the expression

$$\chi_s = \frac{\tilde{g}}{a_0[(T - T^*) + 3T_S\Psi^2]}, \qquad (2)$$

where $T_S = 158$ K, $T^* = 105$ K, and $a_0 \sim 0.093$. The GL analysis presented in the Appendix shows that the fitting parameter a_0 arises from the GL quadratic term $a\Psi^2/2$ in a second-order transition where $a = a_0(T - T^*)$. Ψ is the equilibrium value of the spin nematic order parameter from the unrestricted MC simulations [red, Fig. 1(a)] and it is temperature dependent. For $T \geqslant T_S$, Ψ vanishes and χ_s exhibits Curie-Weiss behavior, in excellent agreement with the experimental χ^{exp} [22].

Let us discuss the meaning of the parameter T^*:

(1) From Fig. 1(b), the unrestricted numerical results at the critical temperature T_S indicate a linear relation between Ψ and ϵ, while individually both behave as order parameters; i.e., they change fast near T_S. The lattice distortion is temperature dependent, i.e., $\epsilon = \epsilon(T)$, because the lattice is equilibrated together with the spins. However, this nearly temperature independent ratio $\Psi/\epsilon = K$ (∼360) depends on couplings: comparing results at several values of the coupling $\tilde{g}$, it is empirically concluded that $K = \frac{\hat{c}}{\tilde{g}}$ (where $\hat{c}$ is a constant).

Note also that χ_s depends on the partial derivative $\partial\Psi/\partial\epsilon|_{\epsilon_0}$, since χ_s is obtained at a constant temperature varying ϵ via strain to match the procedure followed in experiments [22], in the vicinity of the equilibrium point ϵ_0 [namely, χ_s arises from the green/blue curves of Fig. 1(b), not from the red equilibrium curve]. While these slopes (restricted vs unrestricted MC) are in general different, both become very similar at temperatures close to T_S where, as shown analytically in the Appendix, these derivatives are indeed almost the same. Thus, at T_S: $\frac{d\Psi}{d\epsilon} = \frac{\hat{c}}{\tilde{g}} \approx \frac{\partial\Psi}{\partial\epsilon}|_{\epsilon_0} = \chi_s$. This relation can be independently deduced from the GL analysis, Eq. (A18), with $\hat{c} = c_0$, and c_0 arising from $c_0\epsilon^2/2$ in the free energy, providing physical meaning to parameters in the computational fits.

(2) Since the numerical susceptibility χ_s can be fitted well by Eq. (A40) including the special case of T_S where $\Psi = 0$; then, as shown in the Appendix, $T_S = T^* + \frac{\tilde{g}^2}{a_0\hat{c}}$ [22,30]. Comparing with Eq (A21), $\hat{c}$ is again identified with the uncoupled shear elastic modulus c_0. In addition, from previous investigations [17] it is known that at $\tilde{g} = \tilde{\lambda} = 0$ there is no nematic regime and $T_S = T_N$, the Néel temperature. Then, $T_N = T^* + \frac{\tilde{g}^2}{a_0 c_0}$, which at $\tilde{g} = 0$ leads to the important conclusion that the scale T^* is simply equal to the Néel temperature of the purely electronic spin fermion model. In previous work [17] it was reported that T_N at $\tilde{g} = \tilde{\lambda} = 0$ is ∼100–110 K, in remarkable agreement with the fitting value of T^* obtained independently. Thus, in the Curie-Weiss formula T^* is solely determined by the magnetic properties of the purely electronic system.

An important comment is here in order. In principle, by symmetry considerations it is to be expected that all operators with the same B_{1g} symmetry, as Ψ, Φ, and ϵ have, will simultaneously develop a nonzero expectation value in the ground state if this state breaks spontaneously the B_{1g} symmetry as in the case of the $(\pi,0)$ antiferromagnetic state. However, the magnitude of these expectation values can be used as an indicator of which one dominates. For instance, although the lattice (ϵ) does develop a distortion in experiments, its value is widely considered to be too "small" to assume that the lattice is the driver. Consider now the spin and orbital: for results corresponding to our model see Fig. 3 of Ref. [14]. That figure contains the expectation values of Ψ (spin) and Φ (orbital) vs temperature. The important point is that in the temperature range of that figure the expectation value of Ψ is already a large fraction of the low-temperature result, but in the same temperature range Φ had to be multiplied by 10 to magnify its value to become more visible. Thus, based on these relative values considerations we arrive at the

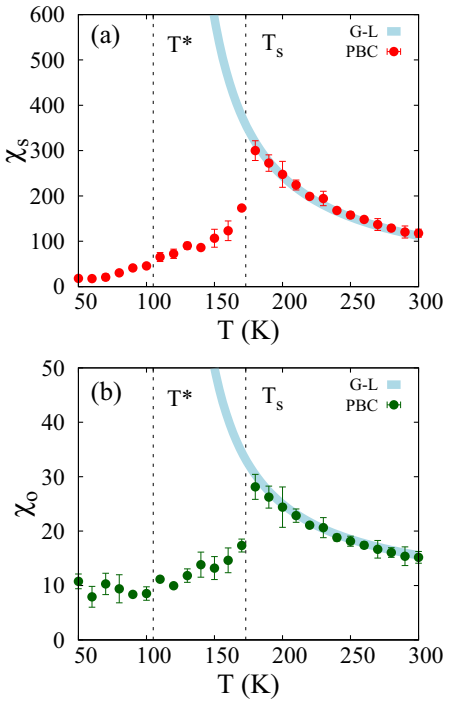

FIG. 3. (Color online) (a) The spin and (b) orbital nematic susceptibility obtained from Monte Carlo simulations for $\tilde{\alpha} = 0.0011$, $\tilde{g} = 0.16$, and $\tilde{\lambda} = 0.12$. The continuous curves in light blue are the fittings obtained from the numerically guided Ginzburg-Landau approach.

conclusion that in the spin fermion model the spin dominates more than the orbital.

B. Analysis of χ_o results

The orbital-based nematic susceptibility, $\chi_o = \frac{\partial \Phi}{\partial \epsilon}|_{\epsilon_0}$, was also numerically calculated varying the temperature. For small $\tilde{\lambda}$, such as $\tilde{\lambda} = 0.12$, the result is approximately temperature independent and well fitted by Eq. (A38) in the Appendix, with $e_0 = 0.016$ and $f = 0.33$. In other words, the analog of Fig. 1(b) but for the orbital-nematic order parameter presents blue/green/red curves all with very similar slopes. Then, in χ_o there is no Curie-Weiss behavior for $T \geqslant T_S$. However, Raman scattering studies of charge nematic fluctuations in $BaFe_2As_2$ and $Sr(Fe_{1-x}Co_x)_2As_2$ have reported Curie-Weiss behavior in the orbital-nematic susceptibility that was well fitted by the expression $a + \frac{b}{T-T_0}$, where a represents the temperature-independent flat continuum and the Curie-Weiss term describes the diverging behavior of the quasielastic peak observed in the Raman spectrum [31].

To reproduce these results with the spin fermion model we considered a small direct coupling $\tilde{\alpha}$ between the magnetic and orbital degrees of freedom, and introduce a new term in the model

$$H_{SO} = -\tilde{\alpha} \sum_{\mathbf{i}} \Psi_{\mathbf{i}} \Phi_{\mathbf{i}}. \tag{3}$$

In Fig. 3(a) the spin-nematic susceptibility is displayed after repeating the simulation in the presence of this new coupling, and it can be seen that its qualitative form is not affected by the inclusion of a small $\tilde{\alpha} = 0.0011$. However, the orbital susceptibility shown in panel (b) of the same figure now displays Curie-Weiss behavior induced by the new coupling between the orbital and magnetic degrees of freedom. The numerical data are well fitted by the expression

$$\chi_o = \frac{\tilde{\lambda}}{e_0} + \frac{\tilde{\alpha}(\tilde{g}e_0 + \tilde{\lambda}\tilde{\alpha})}{a_0 e_0^2 \left[T - \left(T^* + \frac{\tilde{\alpha}^2}{a_0 e_0}\right)\right]}, \tag{4}$$

which has the form $a + \frac{b}{T-T_0}$ used in Ref. [31] to fit the experimental data. Notice that Eq. (4) has been obtained with the GL approach described in the Appendix.

The difference between T^* and T_0 is only about 10 K for the parameters used here. In other words, if a direct coupling between the magnetic and orbital degrees of freedom is present, the Curie-Weiss divergence still occurs at the Néel temperature for the purely electronic system now given by T_0. These results demonstrate how experimental data obtained with different techniques can all be well reproduced by the spin fermion model studied here.

V. T_S VERSUS $\tilde{\lambda}$

The study in Figs. 1(a) and 1(b) was repeated for other values of the coupling $\tilde{\lambda}$. It was observed that $\hat{c}$ varies with $\tilde{\lambda}$, compatible with the GL analysis where $c(\tilde{\lambda}) = c_0(1 - \frac{\tilde{\lambda}^2}{e_0 c_0})$, Eq. (A35). At small $\tilde{\lambda}$, the total (unrestricted MC) and partial (restricted MC) derivatives of Ψ with respect to ϵ are still approximately equal at $T \approx T_S$ as shown in the Appendix. Then, $\chi_s \approx c(\tilde{\lambda})/\tilde{g} = \frac{\tilde{g}}{a_0(T_S - T^*)}$, leading to the result

$$T_S = T^* + \frac{\tilde{g}^2}{a_0 c_0 \left(1 - \frac{\tilde{\lambda}^2}{c_0 e_0}\right)}. \tag{5}$$

Numerically, it was found that $a_0 \sim 0.093$, $c_0 \sim 60$, $e_0 = 0.016$, and $T^* = 105$ K, for $\tilde{g} = 0.16$ (note that the values of the various GL parameters are the same in all the fits reported here, as expected). In practice, it was observed that Eq. (5) fits remarkably well the numerical values for T_S in the range of $\tilde{\lambda}$ studied showing that the GL approach provides an excellent rationalization of the numerical results. This is shown explicitly in Fig. 4(a).

VI. SPIN STRUCTURE FACTORS AND PSEUDOGAPS

In Fig. 4(b), the spin structure factors $S(\mathbf{k})$ calculated with MC at both $(\pi,0)$ and $(0,\pi)$ are shown. The results illustrate the development of short-range magnetic order upon cooling with two coexisting wave vectors. Within the error bars, given roughly by the oscillations in the plot, these results indicate that the two wave vectors develop with equal weight upon cooling approximately starting at T_{PG} where the pseudogap develops (see below) [32].

In the spin fermion model, dynamical observables can be easily calculated. In particular, the density of states $N(\omega)$ is shown in Fig. 4(c). This figure indicates the presence of a Fermi-level pseudogap (PG) in a wide temperature range, in agreement with photoemission and infrared experiments [33]. A zero-temperature pseudogap is to be expected: Hartree-Fock studies of the multiorbital Hubbard model [34] already detected such a feature. However, our finite-temperature studies

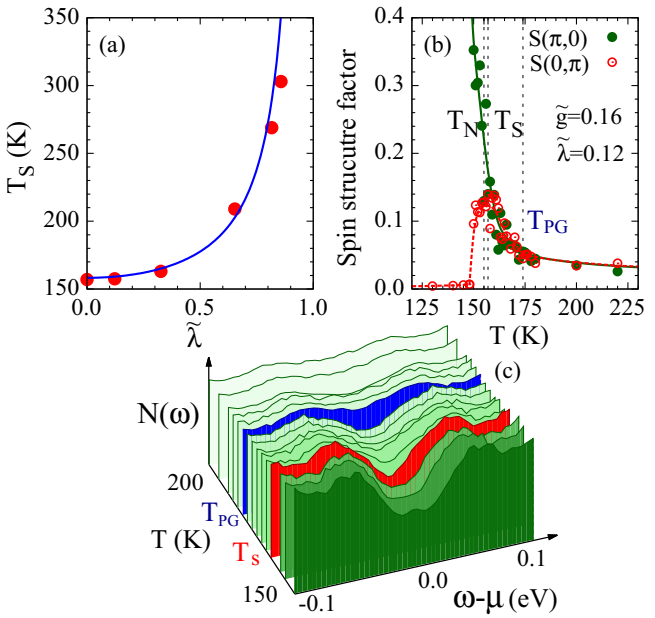

FIG. 4. (Color online) (a) The MC structural transition temperature T_S vs the orbital-lattice coupling $\tilde{\lambda}$, at fixed $\tilde{g} = 0.16$. The continuous line is the fit in Eq. (5), from the GL equations. (b) Spin structure factor $S(\mathbf{k})$ vs temperature T for the two magnetic wave vectors of relevance. Results were obtained via MC simulations on PBC 8×8 clusters. $T_{\rm PG}$ is the pseudogap temperature [Fig. 4(c)]. (c) Density of states $N(\omega)$ (symmetrized) from unrestricted MC simulations on 8×8 clusters ($\tilde{g} = 0.16; \tilde{\lambda} = 0.12$), at various temperatures. Results at $T_S = 158$ K are in red. $T_{\rm PG} \sim 174$ K (blue) is the crossover temperature where the pseudogap opens at the Fermi level (i.e., at $\omega - \mu = 0.0$) upon cooling.

reveal that upon cooling this pseudogap develops at a $T_{\rm PG}$ clearly above T_S. From the analysis of our results, the pseudogap is present when short-range spin correlations are present [Fig. 4(b)]: the "nematic fluctuations" regime is basically the range of temperatures where $(\pi,0)/(0,\pi)$ magnetic fluctuations exist. The coupling to the lattice creates concomitant local orthorhombic distortions: it is important to remark that the region between T_S and $T_{\rm PG}$ is tetragonal only on average [35]. All these results are in good agreement with recent scanning tunneling spectroscopy studies of NaFeAs [36].

VII. CONCLUSIONS

Our combined numerical and analytical study of the spin fermion model leads to results in agreement with the experimentally measured nematic susceptibility of $Ba(Fe_{1-x}Co_x)_2As_2$ [22]. For spins coupled to the lattice our spin-nematic susceptibility has a Curie-Weiss behavior for $T > T_S$ governed by a T^* which we here identify as the critical T_N of the purely electronic sector, which is preexisting to the introduction of the lattice. For realistic nonzero electron-lattice couplings, the lattice induces a nematic/structural transition at a higher temperature T_S. The addition of an orbital-lattice coupling $\tilde{\lambda}$ further increases T_S, with a Curie-Weiss behavior that continues being regulated by T^*. Our main prediction is that whenever fluctuating nematic order is observed, inelastic neutron scattering for the same sample should also reveal the existence of short-range magnetic order: nematic fluctuations, pseudogap, and short-range antiferromagnetic order should all develop simultaneously in these materials. Finally, note that our present results rely on a particular model, the spin fermion model; thus they cannot be considered conclusive proof that magnetism is the driver of nematicity in the real materials. Only further work with other models or via more elaborated experiments can finally settle this matter.

ACKNOWLEDGMENTS

Conversations with Weicheng Lv are acknowledged. C.B. and N.P. were supported by the National Science Foundation, Grant No. DMR-1404375. E.D., A. Moreo, and A. Mukherjee were supported by the US Department of Energy, Office of Basic Energy Sciences, Materials Sciences and Engineering Division.

APPENDIX

This Appendix provides additional detail about results presented in the main text. In particular, it includes the full Hamiltonian, the derivations of equations deduced in the Ginzburg-Landau context, the relationship between partial and total derivatives at T_S, and Monte Carlo results at the (unphysically large [14]) coupling $\tilde{\lambda} = 0.84$.

1. Full Hamiltonian

The full Hamiltonian of the spin fermion model with lattice interactions incorporated is here provided. The same Hamiltonian was also used in Ref. [14]. The model is given by

$$H_{\rm SF} = H_{\rm Hopp} + H_{\rm Hund} + H_{\rm Heis} + H_{\rm SL} + H_{\rm OL} + H_{\rm Stiff}. \quad \text{(A1)}$$

The hopping component is made of three contributions,

$$H_{\rm Hopp} = H_{xz,yz} + H_{xy} + H_{xz,yz;xy}. \quad \text{(A2)}$$

The first term involves the xz and yz orbitals:

$$\begin{aligned} H_{xz,yz} = \Big\{ & -t_1 \sum_{\mathbf{i},\sigma} (d^\dagger_{\mathbf{i},xz,\sigma} d_{\mathbf{i}+\hat{y},xz,\sigma} + d^\dagger_{\mathbf{i},yz,\sigma} d_{\mathbf{i}+\hat{x},yz,\sigma}) - t_2 \sum_{\mathbf{i},\sigma} (d^\dagger_{\mathbf{i},xz,\sigma} d_{\mathbf{i}+\hat{x},xz,\sigma} + d^\dagger_{\mathbf{i},yz,\sigma} d_{\mathbf{i}+\hat{y},yz,\sigma}) \\ & - t_3 \sum_{\mathbf{i},\hat{\mu}\neq\hat{\nu},\sigma} (d^\dagger_{\mathbf{i},xz,\sigma} d_{\mathbf{i}+\hat{\mu}+\hat{\nu},xz,\sigma} + d^\dagger_{\mathbf{i},yz,\sigma} d_{\mathbf{i}+\hat{\mu}+\hat{\nu},yz,\sigma}) + t_4 \sum_{\mathbf{i},\sigma} (d^\dagger_{\mathbf{i},xz,\sigma} d_{\mathbf{i}+\hat{x}+\hat{y},yz,\sigma} + d^\dagger_{\mathbf{i},yz,\sigma} d_{\mathbf{i}+\hat{x}+\hat{y},xz,\sigma}) \\ & - t_4 \sum_{\mathbf{i},\sigma} (d^\dagger_{\mathbf{i},xz,\sigma} d_{\mathbf{i}+\hat{x}-\hat{y},yz,\sigma} + d^\dagger_{\mathbf{i},yz,\sigma} d_{\mathbf{i}+\hat{x}-\hat{y},xz,\sigma}) + \text{H.c.} \Big\} - \mu \sum_{\mathbf{i}} (n_{\mathbf{i},xz} + n_{\mathbf{i},yz}). \end{aligned} \quad \text{(A3)}$$

The second term contains the hoppings related to the xy orbital:

$$H_{xy} = t_5 \sum_{\mathbf{i},\hat{\mu},\sigma} (d^{\dagger}_{\mathbf{i},xy,\sigma} d_{\mathbf{i}+\hat{\mu},xy,\sigma} + \text{H.c.}) - t_6 \sum_{\mathbf{i},\hat{\mu}\neq\hat{\nu},\sigma} (d^{\dagger}_{\mathbf{i},xy,\sigma} d_{\mathbf{i}+\hat{\mu}+\hat{\nu},xy,\sigma} + \text{H.c.}) + \Delta_{xy} \sum_{\mathbf{i}} n_{\mathbf{i},xy} - \mu \sum_{\mathbf{i}} n_{\mathbf{i},xy}. \tag{A4}$$

The last hopping term is

$$\begin{aligned} H_{\text{xz,yz;xy}} = & -t_7 \sum_{\mathbf{i},\sigma} [(-1)^{|\mathbf{i}|} d^{\dagger}_{\mathbf{i},xz,\sigma} d_{\mathbf{i}+\hat{x},xy,\sigma} + \text{H.c.}] - t_7 \sum_{\mathbf{i},\sigma} [(-1)^{|\mathbf{i}|} d^{\dagger}_{\mathbf{i},xy,\sigma} d_{\mathbf{i}+\hat{x},xz,\sigma} + \text{H.c.}] \\ & - t_7 \sum_{\mathbf{i},\sigma} [(-1)^{|\mathbf{i}|} d^{\dagger}_{\mathbf{i},yz,\sigma} d_{\mathbf{i}+\hat{y},xy,\sigma} + \text{H.c.}] - t_7 \sum_{\mathbf{i},\sigma} [(-1)^{|\mathbf{i}|} d^{\dagger}_{\mathbf{i},xy,\sigma} d_{\mathbf{i}+\hat{y},yz,\sigma} + \text{H.c.}] \\ & - t_8 \sum_{\mathbf{i},\sigma} [(-1)^{|\mathbf{i}|} d^{\dagger}_{\mathbf{i},xz,\sigma} d_{\mathbf{i}+\hat{x}+\hat{y},xy,\sigma} + \text{H.c.}] + t_8 \sum_{\mathbf{i},\sigma} [(-1)^{|\mathbf{i}|} d^{\dagger}_{\mathbf{i},xy,\sigma} d_{\mathbf{i}+\hat{x}+\hat{y},xz,\sigma} + \text{H.c.}] \\ & - t_8 \sum_{\mathbf{i},\sigma} [(-1)^{|\mathbf{i}|} d^{\dagger}_{\mathbf{i},xz,\sigma} d_{\mathbf{i}+\hat{x}-\hat{y},xy,\sigma} + \text{H.c.}] + t_8 \sum_{\mathbf{i},\sigma} [(-1)^{|\mathbf{i}|} d^{\dagger}_{\mathbf{i},xy,\sigma} d_{\mathbf{i}+\hat{x}-\hat{y},xz,y\sigma} + \text{H.c.}] \\ & - t_8 \sum_{\mathbf{i},\sigma} [(-1)^{|\mathbf{i}|} d^{\dagger}_{\mathbf{i},yz,\sigma} d_{\mathbf{i}+\hat{x}+\hat{y},xy,\sigma} + \text{H.c.}] + t_8 \sum_{\mathbf{i},\sigma} [(-1)^{|\mathbf{i}|} d^{\dagger}_{\mathbf{i},xy,\sigma} d_{\mathbf{i}+\hat{x}+\hat{y},yz,\sigma} + \text{H.c.}] \\ & + t_8 \sum_{\mathbf{i},\sigma} [(-1)^{|\mathbf{i}|} d^{\dagger}_{\mathbf{i},yz,\sigma} d_{\mathbf{i}+\hat{x}-\hat{y},xy,\sigma} + \text{H.c.}] - t_8 \sum_{\mathbf{i},\sigma} [(-1)^{|\mathbf{i}|} d^{\dagger}_{\mathbf{i},xy,\sigma} d_{\mathbf{i}+\hat{x}-\hat{y},yz,\sigma} + \text{H.c.}]. \end{aligned} \tag{A5}$$

In the equations above, the operator $d^{\dagger}_{\mathbf{i},\alpha,\sigma}$ creates an electron at site $\mathbf{i}$ of the two-dimensional lattice of irons. The orbital index is $\alpha = xz$, yz, or xy, and the z-axis spin projection is σ. The chemical potential used to regulate the electronic density is μ. The symbols $\hat{x}$ and $\hat{y}$ denote vectors along the axes that join NN atoms. The values of the hoppings t_i are from Ref. [23] and they are reproduced in Table I, including also the value of the energy splitting Δ_{xy}.

The remaining terms of the Hamiltonian have been briefly discussed in the main text. The symbols $\langle\rangle$ denote NN while $\langle\langle\rangle\rangle$ denote NNN. The rest of the notation is standard.

$$H_{\text{Hund}} = -J_{\text{H}} \sum_{\mathbf{i},\alpha} \mathbf{S}_{\mathbf{i}} \cdot \mathbf{s}_{\mathbf{i},\alpha}, \tag{A6}$$

$$H_{\text{Heis}} = J_{\text{NN}} \sum_{\langle\mathbf{ij}\rangle} \mathbf{S}_{\mathbf{i}} \cdot \mathbf{S}_{\mathbf{j}} + J_{\text{NNN}} \sum_{\langle\langle\mathbf{im}\rangle\rangle} \mathbf{S}_{\mathbf{i}} \cdot \mathbf{S}_{\mathbf{m}}, \tag{A7}$$

$$H_{\text{SL}} = -g \sum_{\mathbf{i}} \Psi_{\mathbf{i}} \epsilon_{\mathbf{i}}, \tag{A8}$$

$$H_{\text{OL}} = -\lambda \sum_{\mathbf{i}} \Phi_{\mathbf{i}} \epsilon_{\mathbf{i}}, \tag{A9}$$

$$\begin{aligned} H_{\text{Stiff}} = & \frac{1}{2} k \sum_{\mathbf{i}} \sum_{\nu=1}^{4} \left(\left| \mathbf{R}^{\mathbf{i}\nu}_{\text{Fe-As}} \right| - R_0 \right)^2 \\ & + k' \sum_{\langle\mathbf{ij}\rangle} \left[\left(\frac{a_0}{R^{\mathbf{ij}}_{\text{Fe-Fe}}} \right)^{12} - 2 \left(\frac{a_0}{R^{\mathbf{ij}}_{\text{Fe-Fe}}} \right)^{6} \right]. \end{aligned} \tag{A10}$$

TABLE I. Values of the parameters that appear in the tight-binding portion of the three-orbital model Eqs. (A3) to (A5). The overall energy unit is electron volts.

t_1	t_2	t_3	t_4	t_5	t_6	t_7	t_8	Δ_{xy}
0.02	0.06	0.03	−0.01	0.2	0.3	−0.2	0.1	0.4

The $\mathcal{O}_{rth}$ strain $\epsilon_{\mathbf{i}}$ is defined as

$$\epsilon_{\mathbf{i}} = \frac{1}{4\sqrt{2}} \sum_{\nu=1}^{4} \left(\left| \delta^{y}_{\mathbf{i},\nu} \right| - \left| \delta^{x}_{\mathbf{i},\nu} \right| \right), \tag{A11}$$

where $\delta^{x}_{\mathbf{i},\nu}(\delta^{y}_{\mathbf{i},\nu})$ is the component along x (y) of the distance between the Fe atom at site $\mathbf{i}$ of the lattice and one of its four neighboring As atoms that are labeled by the index $\nu = 1,2,3,4$. For more details of the notation used see Ref. [14], where the technical aspects on how to simulate an orthorhombic distortion can also be found.

2. Ginzburg-Landau phenomenological approach

In this section, the Monte Carlo data gathered for the spin fermion model will be described via a phenomenological Ginzburg-Landau (GL) approach, to provide a more qualitative description of those numerical results. More specifically, the free energy F of the spin fermion model will be (approximately) written in terms of the spin-nematic order parameter Ψ, the orbital-nematic order parameter Φ, and the orthorhombic strain ϵ, as in GL descriptions. In previous literature a single nematic order parameter was considered without separating its magnetic and orbital character [22,30,37]. In addition, it was necessary to formulate assumptions about the order of the nematic and structural transitions. In our case, the MC results in this and previous publications are used as guidance to address this matter at the free energy level. More specifically, a second-order magnetic transition was previously reported for the purely electronic system [17]. Thus, the spin-nematic portion of F should display a free energy with a second-order phase transition.

With regards to the terms involving ϵ, the MC results of Ref. [14] showed that the coupling of the spin-nematic order parameter to the lattice leads to a weak first-order (or very sharp second-order) nematic and structural transition. Naively, this implies that the order ϵ^4 term should have a negative coefficient. However, since in our numerical simulations a

Lennard-Jones potential is used for the elastic term, then the sign of the quartic term is fixed and it happens to be positive. However, considering that the ϵ displacements are very small and the transition is weakly first order at best, then just the harmonic (second-order) approximation should be sufficient for ϵ.

After all these considerations, the free energy is given by

$$F = \frac{a}{2}\Psi^2 + \frac{b}{4}\Psi^4 + \frac{c}{2}\epsilon^2 + \frac{e}{2}\Phi^2 + \frac{f}{4}\Phi^4 \quad \text{(A12)}$$

$$-\tilde{g}\Psi\epsilon - \tilde{\lambda}\Phi\epsilon - h\epsilon, \quad \text{(A13)}$$

where a, b, c, e, and f are the coefficients of the many terms of the three order parameters, while $\tilde{g}$ and $\tilde{\lambda}$ are the coupling constants of the lattice with the spin and orbital degrees of freedom as described in the main text. Since this and previous MC studies [14,17] showed that there is no long-range orbital order in the ground state of the spin fermion model, at least in the range of couplings investigated, then a positive quartic term is used for this order parameter. The parameter h denotes an external stress, as explained in Ref. [22]. Note that in principle another term, and associated coupling constant, $\tilde{\alpha}\Psi\Phi$ should be included in F. This term will affect the orbital susceptibility and its effects will be described at the end of this subsection.

As explained in the main text, our MC results indicate that the leading order parameter guiding the results is the spin-nematic Ψ. Thus, it is reasonable to assume that only the coefficient a depends on temperature as $a = a_0(T - T^*)$, while other parameters, such as $c = c_0$ (the uncoupled shear elastic modulus) and $e = e_0$, are approximately temperature independent.

For the special case $\tilde{g} = \tilde{\lambda} = 0$ the critical temperature T^* for the magnetic transition can be obtained by setting to zero the derivative of F with respect to Ψ:

$$\frac{\partial F}{\partial \Psi} = a\Psi + b\Psi^3 = 0. \quad \text{(A14)}$$

Then, for $T \leqslant T^*$ the order parameter is given by

$$\Psi = \sqrt{\frac{a_0}{b}(T^* - T)}. \quad \text{(A15)}$$

The equation above is valid only when Ψ is small, i.e., close to the transition temperature from below. Additional terms in the free energy would be needed as $T \to 0$ since in that limit $|\Psi| = 2$.

Now consider the case when $\tilde{g}$ is nonzero, still keeping $\tilde{\lambda} = 0$. Setting to zero the derivative of F with respect to Ψ and ϵ leads to (for $h = 0$)

$$\frac{\partial F}{\partial \epsilon} = c_0\epsilon - \tilde{g}\Psi = 0, \quad \text{(A16)}$$

$$\frac{\partial F}{\partial \Psi} = a\Psi + b\Psi^3 - \tilde{g}\epsilon = 0. \quad \text{(A17)}$$

From Eq. (A16),

$$\Psi = \frac{c_0}{\tilde{g}}\epsilon, \quad \text{(A18)}$$

which reproduces the linear relation obtained numerically before, see Fig. 1(b) main text, with a slope now explicitly given in terms of $\tilde{g}$ and a constant that now can be identified with the bare shear elastic modulus c_0.

Solving for ϵ in Eq. (A17) and introducing the result in Eq. (A16) leads to

$$\left(a - \frac{\tilde{g}^2}{c_0}\right)\Psi + b\Psi^3 = 0, \quad \text{(A19)}$$

where it is clear that a becomes renormalized due to the coupling to the lattice. The transition now occurs at a renormalized temperature T_S that satisfies

$$a_0(T - T_S) = a - \frac{\tilde{g}^2}{c_0} = a_0(T - T^*) - \frac{\tilde{g}^2}{c_0}. \quad \text{(A20)}$$

From the expression above, it can be shown that the new nematic transition occurs at

$$T_S = T^* + \frac{\tilde{g}^2}{a_0 c_0}, \quad \text{(A21)}$$

and clearly $T_S > T^*$. Note that Eq. (A21) has been obtained in previous GL analysis, but in those studies a generic nematic coupling appeared in the numerator of the second term while here, more specifically, we identify $\tilde{g}$ with the spin-nematic coupling to the lattice.

Reciprocally, solving for Ψ in Eq. (A16) and introducing the result in Eq. (A17) leads to

$$\frac{a}{\tilde{g}}\left[\left(c_0 - \frac{\tilde{g}^2}{a}\right)\epsilon + \frac{bc_0^3}{\tilde{g}^2 a}\epsilon^3\right] = 0, \quad \text{(A22)}$$

where, due to the coupling to the lattice, now the shear constant is renormalized and an effective quartic term is generated for the lattice free energy. The effective shear elastic modulus c_{66} becomes temperature dependent and it is given by

$$c_{66} = c_0 - \frac{\tilde{g}^2}{a_0(T - T^*)}, \quad \text{(A23)}$$

which vanishes at $T = T_S$. Thus, the structural transition occurs at the same critical temperature T_S of the nematic transition.

To obtain the spin-nematic susceptibility, the second derivative of F with respect to Ψ and h is set to zero:

$$\frac{\partial^2 F}{\partial h \partial \Psi} = a\frac{\partial \Psi}{\partial h} + 3b\Psi^2\frac{\partial \Psi}{\partial h} - \tilde{g}\frac{\partial \epsilon}{\partial h} = 0, \quad \text{(A24)}$$

and then

$$\chi_s = \frac{\partial \Psi}{\partial \epsilon} = \frac{\frac{\partial \Psi}{\partial h}}{\frac{\partial \epsilon}{\partial h}} = \frac{\tilde{g}}{a + 3b\Psi^2} = \frac{\tilde{g}}{a_0(T - T^*) + 3b\Psi^2}. \quad \text{(A25)}$$

This is an important equation that was used in the main text to rationalize the MC numerical results. In the range $T \geqslant T_S$, i.e., when $\Psi = 0$, the spin-nematic susceptibility clearly follows a Curie-Weiss behavior. In practice, it has been observed that $b = a_0 T_S$ to a good approximation.

Consider now the case when the orbital-lattice coupling $\tilde{\lambda}$ is nonzero as well. Now

$$\frac{\partial F}{\partial \epsilon} = c_0\epsilon - \tilde{g}\Psi - \tilde{\lambda}\Phi = 0, \quad \text{(A26)}$$

$$\frac{\partial F}{\partial \Psi} = a\Psi + b\Psi^3 - \tilde{g}\epsilon = 0, \quad \text{(A27)}$$

and a new equation is available:

$$\frac{\partial F}{\partial \Phi} = e_0\Phi + f\Phi^3 - \tilde{\lambda}\epsilon = 0. \tag{A28}$$

Solving for Ψ in Eq. (A26) leads to

$$\Psi = \frac{c_0\epsilon - \tilde{\lambda}\Phi}{\tilde{g}}, \tag{A29}$$

while solving for ϵ in Eq. (A27) leads to

$$\epsilon = \frac{a\Psi + b\Psi^3}{\tilde{g}}. \tag{A30}$$

Introducing Eq. (A30) into Eq. (A29), Φ is obtained in terms of Ψ as follows:

$$\Phi = \left(\frac{c_0}{\tilde{\lambda}\tilde{g}}\right)\left[\left(a - \frac{\tilde{g}^2}{c_0}\right)\Psi + b\Psi^3\right]. \tag{A31}$$

Introducing Eqs. (A30) and (A31) into Eq. (A28) a renormalized equation for Ψ is obtained:

$$\left[\frac{e_0c_0}{\tilde{\lambda}\tilde{g}}\left(a - \frac{\tilde{g}^2}{c_0}\right) - \frac{\tilde{\lambda}a}{\tilde{g}}\right]\Psi + \left[\frac{e_0c_0}{\tilde{\lambda}\tilde{g}}b - \frac{\tilde{\lambda}b}{\tilde{g}} + \frac{fc_0^3}{\tilde{\lambda}^3\tilde{g}^3}\left(a - \frac{\tilde{g}^2}{c_0}\right)^3\right]\Psi^3 = 0. \tag{A32}$$

Then, at $T = T_S$ the effective coefficient of the linear term in Ψ provides the new transition temperature:

$$a_0(T - T_S) = a - \frac{e_0\tilde{g}^2}{e_0c_0 - \tilde{\lambda}^2}. \tag{A33}$$

Using that $a = a_0(T - T^*)$, the dependence of the critical temperature with the two coupling constants $\tilde{g}$ and $\tilde{\lambda}$ can be obtained:

$$T_S = T^* + \frac{\tilde{g}^2}{a_0c_0\left(1 - \frac{\tilde{\lambda}^2}{c_0e_0}\right)}. \tag{A34}$$

This is another interesting formula that nicely describes the MC results, as shown in the main text. Equation (A34) shows that T_S depends in a different way on the spin-lattice ($\tilde{g}$) and the orbital-lattice ($\tilde{\lambda}$) couplings. Moreover, an effective $\tilde{\lambda}$-dependent elastic modulus $c(\tilde{\lambda})$ can be defined as

$$c(\tilde{\lambda}) = c_0 - \frac{\tilde{\lambda}^2}{e_0}. \tag{A35}$$

In addition, the effective shear elastic modulus is now given by

$$c_{66} = c_0 - \frac{\tilde{\lambda}^2}{e_0} - \frac{\tilde{g}^2}{a_0(T - T^*)}, \tag{A36}$$

which vanishes at the T_S given by Eq. (A34).

The spin-nematic susceptibility is still given by Eq. (A25) with the dependence on $\tilde{\lambda}$ embedded in the actual values of Ψ. The orbital-nematic susceptibility is obtained from Eq. (A28) as

$$\frac{\partial^2 F}{\partial h \partial \Phi} = (e_0 + 3f\Phi^2)\frac{\partial \Phi}{\partial h} - \tilde{\lambda}\frac{\partial \epsilon}{\partial h} = 0. \tag{A37}$$

In the absence of an explicit coupling $\tilde{\alpha}$ between the spin-nematic and orbital order parameters, then the orbital-nematic susceptibility becomes

$$\chi_o = \frac{\partial \Phi}{\partial \epsilon} = \frac{\frac{\partial \Phi}{\partial h}}{\frac{\partial \epsilon}{\partial h}} = \frac{\tilde{\lambda}}{e_0 + 3f\Phi^2}. \tag{A38}$$

If a term of the form $\tilde{\alpha}\Psi\Phi$ is added to the free energy, as discussed in the main text, the expressions for the susceptibilities can be obtained for $T \geqslant T_S$. The orbital susceptibility now displays Curie-Weiss behavior:

$$\chi_o = \frac{\tilde{\lambda}}{e_0} + \frac{\tilde{\alpha}(\tilde{g}e_0 + \tilde{\lambda}\tilde{\alpha})}{a_0e_0^2\left[T - \left(T^* + \frac{\tilde{\alpha}^2}{a_0e_0}\right)\right]}, \tag{A39}$$

while the spin-nematic susceptibility becomes

$$\chi_s = \frac{\tilde{g}e_0 + \tilde{\lambda}\tilde{\alpha}}{a_0e_0\left[T - \left(T^* + \frac{\tilde{\alpha}^2}{a_0e_0}\right)\right]}, \tag{A40}$$

and the structural transition temperature is given by

$$T_S = T^* + \frac{\tilde{\alpha}^2}{a_0e_0} + \frac{(\tilde{\lambda}\tilde{\alpha} + e_0\tilde{g})^2}{a_0e_0c_0^2\left(1 - \frac{\tilde{\lambda}^2}{e_0c_0}\right)}. \tag{A41}$$

3. Partial and total derivatives at T_S

The partial derivative in the definition of χ_s is at constant temperature varying ϵ and it is evaluated at equilibrium $\epsilon = \epsilon_0$. The slopes of the green and blue curves of Fig. 1(b) in the main text provide this derivative. On the other hand, the results of Fig. 1(b) in equilibrium (slope of the red points curve) provide the full derivative $\frac{d\Psi}{d\epsilon}$. Since $\epsilon = \epsilon(T)$, their relation is

$$\frac{d\Psi}{d\epsilon} = \frac{\partial \Psi}{\partial \epsilon}\bigg|_{\epsilon_0} + \frac{\partial \Psi}{\partial T}\bigg|_{\epsilon_0}\frac{\partial T}{\partial \epsilon}|_{\epsilon_0} = \chi_s + \frac{\frac{\partial \Psi}{\partial T}|_{\epsilon_0}}{\frac{\partial \epsilon}{\partial T}|_{\epsilon_0}}, \tag{A42}$$

where $\frac{\partial \Psi}{\partial T}$ is performed at constant ϵ and $\frac{\partial \epsilon}{\partial T}|_{\epsilon_0}$ is performed at constant Ψ. In general, the partial and total derivatives of Ψ with respect to ϵ can differ from one another. However, at small $\tilde{\lambda}$ the structural transition is weakly first order [14] (or a very sharp second order) and then when $T \approx T_S$ the lattice distortion ϵ rapidly jumps from 0 to a finite value. This means that $\frac{\partial \epsilon}{\partial T}|_{\epsilon_0}$ is very large while $\frac{\partial \Psi}{\partial T}|_{\epsilon_0}$ remains finite since it is performed at fixed ϵ. Thus, at $T \approx T_S$, the partial and total derivatives are almost the same. This can be seen in Fig. 1(b) of the main text where the slopes of the green curves at $\epsilon = 0$, when they cross the equilibrium line, are smaller than the equilibrium slope K but increase with decreasing temperature until it becomes equal to K at $T = T_S$ (red line). The slopes of the blue curves at the finite value of ϵ where they cross the equilibrium line are smaller than K and decrease with decreasing temperature.

4. Spin-nematic susceptibility at large $\tilde{\lambda}$

To investigate in more detail the potential role of orbital order in the spin-nematic susceptibility, simulations were repeated for a robust $\tilde{\lambda} = 0.84$, keeping the other electron-lattice coupling fixed as $\tilde{g} = 0.16$. Results are shown in Fig. 5. The increase of $\tilde{\lambda}$ substantially increases T_S, which is to be expected since now the electron-lattice coupling is larger [14]. However, above T_S still the results can be well fitted by a Curie-Weiss law, with a divergence at T^* which is the critical

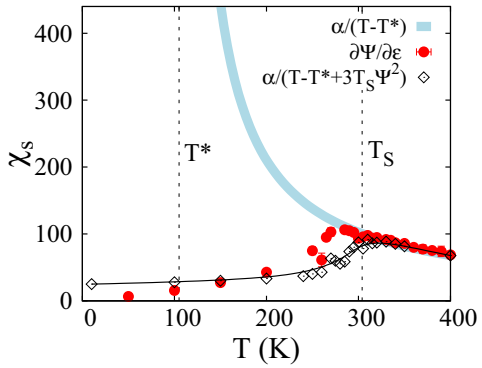

FIG. 5. (Color online) Spin-nematic susceptibility χ_s vs temperature T (red circles) obtained from Fig. 6(b) (at $\tilde{g} = 0.16$ and $\tilde{\lambda} = 0.84$). The standard MC technique on an 8×8 cluster with PBC was employed (involving ED of the fermions at every MC step). Also shown are two GL fits, as also employed in Fig. 2. The blue (thick) line indicates a divergence at a temperature T^* (lower than T_S) characteristic of the electronic sector alone. In the range $T \leqslant T_S$, the lattice follows the electronic behavior. The black (thin) line and black tilted square points are a fit including the $3T_S\Psi^2$ correction (see text in the previous section of this appendix). The fitting parameters are $T^* = 105$ K and $T_S = 304$ K. The actual Néel temperature for $\tilde{g} = 0.16$ and $\tilde{\lambda} = 0.84$ is not shown.

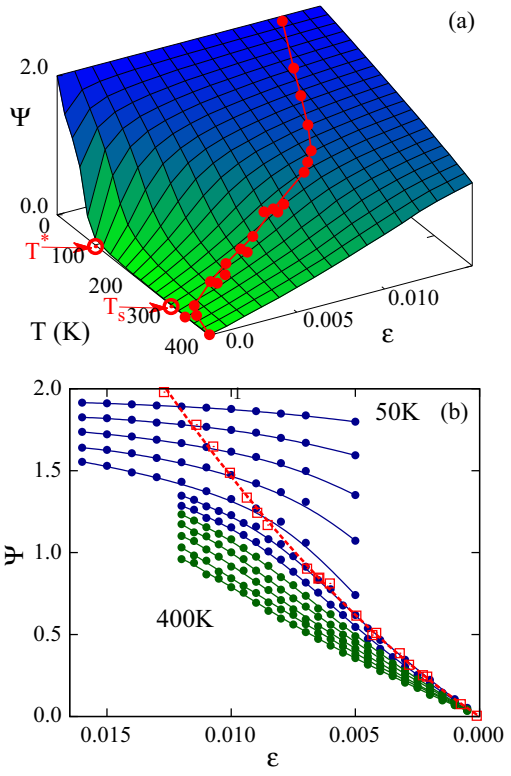

FIG. 6. (Color online) Spin-nematic order parameter from the MC simulations, at $\tilde{g} = 0.16$ and $\tilde{\lambda} = 0.84$. (a) Ψ vs T and ϵ, measured at a fixed lattice distortion ϵ for each temperature (restricted MC). Shown are the T^* temperature (see text) and T_S. Results shown are for an 8×8 cluster with TCA+TBC, but PBC 8×8 clusters with ED give similar results. Red points are the equilibrium values using unrestricted MC with ED and PBC 8×8 clusters. (b) MC results illustrating the relation between Ψ and ϵ in unrestricted MC (red) and the restricted MC curves (green/blue), parametric with temperature. Results are obtained with ED/PBC 8×8 clusters. Note that Ψ vs ϵ (red squares) is no longer linear which is expected because Eq. (A18) is valid only for $\tilde{\lambda} = 0$ (and approximately valid for small $\tilde{\lambda}$).

temperature of the purely electronic system, as described in the main text. Even the coefficient a_0 in the fit is almost identical to that of the case $\tilde{\lambda} = 0.12$, in Fig. 2. The second fit, with the $3T_S\Psi^2$ correction, is still reasonable. In summary, as long as $\tilde{\lambda}$ is not increased to such large values that the low-temperature ground state is drastically altered, the computational results can still be analyzed via the GL formalism outlined here and in the main text, with a T^* that originates in the $(\pi,0)$ magnetic transition of the purely electronic sector. For completeness, the plots analogous to those of Fig. 1 but in the present case of $\tilde{\lambda} = 0.84$ are provided in Fig. 6.

[1] D. C. Johnston, Adv. Phys. **59**, 803 (2010).
[2] P. Dai, J.-P. Hu, and E. Dagotto, Nat. Phys. **8**, 709 (2012).
[3] J-H. Chu, J. G. Analytis, K. De Greve, P. L. McMahon, Z. Islam, Y. Yamamoto, and I. R. Fisher, Science **329**, 824 (2010); see also I. R. Fisher, L. Degiorgi, and Z. X. Shen, Rep. Prog. Phys. **74**, 124506 (2011).
[4] E. Fradkin, S. A. Kivelson, M. J. Lawler, J. P. Eisenstein, and A. P. Mackenzie, Annu. Rev. Condens. Matter Phys. **1**, 153 (2010).
[5] R. M. Fernandes, L. H. VanBebber, S. Bhattacharya, P. Chandra, V. Keppens, D. Mandrus, M. A. McGuire, B. C. Sales, A. S. Sefat, and J. Schmalian, Phys. Rev. Lett. **105**, 157003 (2010).
[6] C. Fang, H. Yao, W.-F. Tsai, J. P. Hu, and S. A. Kivelson, Phys. Rev. B **77**, 224509 (2008).
[7] C. Xu, M. Müller, and S. Sachdev, Phys. Rev. B **78**, 020501(R) (2008).
[8] R. M. Fernandes, A. V. Chubukov, J. Knolle, I. Eremin, and J. Schmalian, Phys. Rev. B **85**, 024534 (2012).
[9] R. M. Fernandes, A. V. Chubukov, and J. Schmalian, Nat. Phys. **10**, 97 (2014).
[10] C.-C. Lee, W.-G. Yin, and Wei Ku, Phys. Rev. Lett. **103**, 267001 (2009).
[11] C.-C. Chen, B. Moritz, J. van den Brink, T. P. Devereaux, and R. R. P. Singh, Phys. Rev. B **80**, 180418(R) (2009); C.-C. Chen, J. Maciejko, A. P. Sorini, B. Moritz, R. R. P. Singh, and T. P. Devereaux, *ibid.* **82**, 100504(R) (2010).
[12] W. Lv, J. S. Wu, and P. Phillips, Phys. Rev. B **80**, 224506 (2009); W.-C. Lee, W. Lv, J. M. Tranquada, and P. W. Phillips, *ibid.* **86**, 094516 (2012).
[13] H. Kontani, Y. Inoue, T. Saito, Y. Yamakawa, and S. Onari, Solid State Commun. **152**, 718 (2012); H. Kontani, T. Saito, and S. Onari, Phys. Rev. B **84**, 024528 (2011).

[14] S. Liang, A. Moreo, and E. Dagotto, Phys. Rev. Lett. **111**, 047004 (2013).

[15] W.-G. Yin, C.-C. Lee, and W. Ku, Phys. Rev. Lett. **105**, 107004 (2010).

[16] W. Lv, F. Krüger, and P. Phillips, Phys. Rev. B **82**, 045125 (2010).

[17] S. Liang, G. Alvarez, C. Sen, A. Moreo, and E. Dagotto, Phys. Rev. Lett. **109**, 047001 (2012).

[18] E. Dagotto, T. Hotta, and A. Moreo, Phys. Rep. **344**, 1 (2001).

[19] H. Gretarsson, A. Lupascu, J. Kim, D. Casa, T. Gog, W. Wu, S. R. Julian, Z. J. Xu, J. S. Wen, G. D. Gu, R. H. Yuan, Z. G. Chen, N.-L. Wang, S. Khim, K. H. Kim, M. Ishikado, I. Jarrige, S. Shamoto, J.-H. Chu, I. R. Fisher, and Y-J. Kim, Phys. Rev. B **84**, 100509(R) (2011).

[20] F. Bondino, E. Magnano, M. Malvestuto, F. Parmigiani, M. A. McGuire, A. S. Sefat, B. C. Sales, R. Jin, D. Mandrus, E. W. Plummer, D. J. Singh, and N. Mannella, Phys. Rev. Lett. **101**, 267001 (2008).

[21] $\Delta_{SN} = T_S - T_N$ can be regulated by the electron-orbital coupling $\tilde{\lambda}$ leading to a Δ_{SN} in our model larger than the small values reported for spin systems [see Y. Kamiya, N. Kawashima, and C. D. Batista, Phys. Rev. B **84**, 214429 (2011); A. L. Wysocki, K. D. Belashchenko, and V. P. Antropov, Nat. Phys. **7**, 485 (2011)].

[22] J-H. Chu, H-H. Kuo, J. G. Analytis, and I. R. Fisher, Science **337**, 710 (2012); Hsueh-Hui Kuo, Maxwell C. Shapiro, Scott C. Riggs, and Ian R. Fisher, Phys. Rev. B **88**, 085113 (2013); and references therein.

[23] M. Daghofer, A. Nicholson, A. Moreo, and E. Dagotto, Phys. Rev. B **81**, 014511 (2010).

[24] The original definitions of Ψ and ϵ in Ref. [14] have been multiplied by -1 so that Ψ and ϵ are both positive here, as assumed in the GL analysis.

[25] The spin in $H_{\rm SL}$ will only be the localized spin for computational simplicity.

[26] S. Kumar and P. Majumdar, Eur. Phys. J. B **50**, 571 (2006).

[27] In unrestricted MC employing the ED method on 8×8 clusters, typically 8 000 thermalization (Th) and up to 100 000 measurement (Ms) steps were used. In restricted MC with ED and 8×8 clusters, the numbers are 8 000 and 20 000 for Th and Ms steps. In restricted MC using TCA+TBC, 4 000 Th and 4 000 Ms steps were employed for a 16×16 cluster with a 4×4 cluster for the MC updates, while for an 8×8 (same MC update cluster) the numbers were 20 000 for Th and 20 000 for Ms steps.

[28] J. Salafranca, G. Alvarez, and E. Dagotto, Phys. Rev. B **80**, 155133 (2009).

[29] The value of T^* is not the same (but close) for 8×8 and 16×16 lattices due to size effects. Then, the fits for each lattice size are carried out with the T^* of each cluster.

[30] S. Kasahara, H. J. Shi, K. Hashimoto, S. Tonegawa, Y. Mizukami, T. Shibauchi, K. Sugimoto, T. Fukuda, T. Terashima, A. H. Nevidomskyy, and Y. Matsuda, Nature (London) **486**, 382 (2012).

[31] Y.-X. Yang, Y. Gallais, R. M. Fernandes, I. Paul, L. Chauvière, M.-A. Méasson, M. Cazayous, A. Sacuto, D. Colson, and A. Forget, JPS Conf. Proc. **3**, 015001 (2014).

[32] Note that in the presence of external strain to detwin crystals, some remaining artificial anisotropy may incorrectly suggest that $(\pi,0)$-$(0,\pi)$ are not degenerate above T_S in neutron scattering, leading to the incorrect conclusion that $T_{\rm PG}$ is T_S (for related observations see C. Dhital, Z. Yamani, Wei Tian, J. Zeretsky, A. S. Sefat, Ziqiang Wang, R. J. Birgeneau, and S. D. Wilson, Phys. Rev. Lett. **108**, 087001 (2012); E. C. Blomberg, A. Kreyssig, M. A. Tanatar, R. M. Fernandes, M. G. Kim, A. Thaler, J. Schmalian, S. L. Bud'ko, P. C. Canfield, A. I. Goldman, and R. Prozorov, Phys. Rev. B **85**, 144509 (2012)).

[33] Our results should be compared against the photoemission experiments reported by T. Shimojima, T. Sonobe, W. Malaeb, K. Shinada, A. Chainani, S. Shin, T. Yoshida, S. Ideta, A. Fujimori, H. Kumigashira, K. Ono, Y. Nakashima, H. Anzai, M. Arita, A. Ino, H. Namatame, M. Taniguchi, M. Nakajima, S. Uchida, Y. Tomioka, T. Ito, K. Kihou, C. H. Lee, A. Iyo, H. Eisaki, K. Ohgushi, S. Kasahara, T. Terashima, H. Ikeda, T. Shibauchi, Y. Matsuda, and K. Ishizaka, Phys. Rev. B **89**, 045101 (2014) (see for instance their Fig. 6). Infrared studies correlating the presence of a pseudogap with antiferromagnetic fluctuations can also be found in S. J. Moon, A. A. Schafgans, S. Kasahara, T. Shibauchi, T. Terashima, Y. Matsuda, M. A. Tanatar, R. Prozorov, A. Thaler, P. C. Canfield, A. S. Sefat, D. Mandrus, and D. N. Basov, Phys. Rev. Lett. **109**, 027006 (2012).

[34] Rong Yu, Kien T. Trinh, Adriana Moreo, Maria Daghofer, José Riera, Stephan Haas, and Elbio Dagotto, Phys. Rev. B **79**, 104510 (2009).

[35] J. L. Niedziela, M. A. McGuire, and T. Egami, Phys. Rev. B **86**, 174113 (2012), and references therein.

[36] E. P. Rosenthal, E. F. Andrade, C. J. Arguello, R. M. Fernandes, L. Y. Xing, X. C. Wang, C. Q. Jin, A. J. Millis, and A. N. Pasupathy, Nat. Phys. **10**, 225 (2014).

[37] R. M. Fernandes and J. Schmalian, Supercond. Sci. Technol. **25**, 084005 (2012).